CHEMISTRY OF MATERIALS

pubs.acs.org/cm

Article

Stable and Efficient Ir Nanoshells for Oxygen Reduction and Evolution Reactions

Alexandre C. Foucher,[▽] Daniel J. Rosen,[▽] Shengsong Yang, Dario Ferreira Sanchez, Ilia Sadykov, Daniel Grolimund, Anatoly I. Frenkel, Christopher B. Murray,* and Eric A. Stach*

Cite This: *Chem. Mater.* 2023, 35, 4572−4580

Read Online

ACCESS | Metrics & More | Article Recommendations | Supporting Information

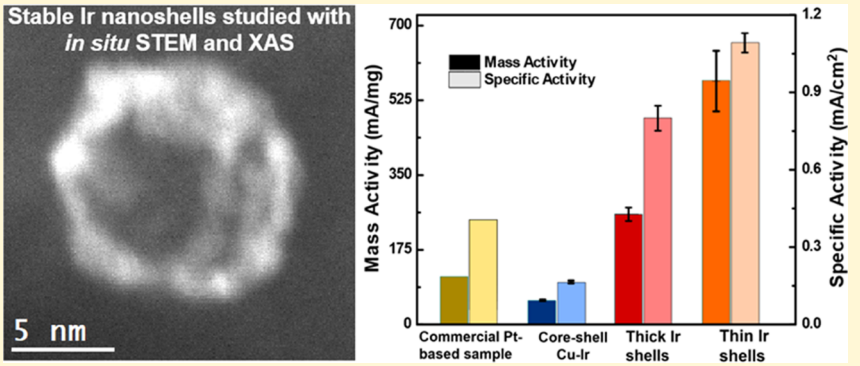

ABSTRACT: We report the characterization and applications of core−shell Cu−Ir nanocatalysts for oxygen reduction reaction and oxygen evolution reaction. Core−shell Cu−Ir particles with tunable thickness of Ir can be oxidized to remove the Cu core and obtain Ir shells. The thickness of the Ir shells determines the stability and optimization of the precious metals. We showed with *in situ* scanning transmission electron microscopy the remarkable stability of the Ir shells at elevated temperatures under oxidative and reductive environments. *In situ* scanning transmission electron microscopy and *in situ* X-ray absorption spectroscopy also showed that traces of remaining copper could be detected in the Ir shells. Electrochemical measurements for oxygen reduction and evolution reactions show promising activity and stability compared to a commercial catalyst. Thin Ir shells, with high surface area per gram of Ir, were more active but less stable than thicker shells. In contrast, thicker Ir shells were more stable and had excellent electrochemical properties in aqueous and alkaline environments. Hence, Ir nanoshells appear as interesting candidates for reducing the cost of catalysis while improving chemical performance in fuel cells.

INTRODUCTION

Heterogeneous catalysis plays a crucial role in major industrial processes.[1] More specifically, catalysts are essential for important chemical reactions, such as the oxygen reduction reaction (ORR) or the oxygen evolution reaction (OER).[2−4] In general, Pt is most commonly used, although other precious metals, such as Ir, can be chosen.[5−10] For instance, it has been shown that Ir can outperform Pt for OER in some conditions.[11,12] Additionally, Pt particles can sometimes easily sinter, which ultimately reduces their catalytic potential.[13] Finally, Pt is in high demand in the field of catalysis, so it is necessary to expand the range of materials that can replace Pt. One issue with Pt or Ir is the high cost of these nanocatalysts, which is a hurdle for expanding the use of fuel cells.[14,15] It is, therefore, necessary to design new nanostructures that can reconcile the need for high activity and high stability[16] while the amount of expensive metal is reduced. To this end, nanoshells and nanocages became interesting candidates. Many methods to form hollow structures have been reported, such as the use of a sacrificial template,[17] the galvanic replacement of a metallic core,[18] or electrodeposition.[19] Additionally, the precipitation of a precursor on monometallic particles in ethanol solvent is also a method to form core−shell particles.[20] Finally, another option is the solvothermal synthesis of core−shell nanoparticles with the removal of the core through oxidation in a solvent.[21] The solvothermal synthesis of core−shell particles is particularly relevant, as it offers great control over the desired hollow structures' size, shape, and composition.[22,23] It is also an easy method that does not waste large quantities of expensive metal precursors.

Previous investigations have focused on hollow or core−shell Ir-based nanostructures as efficient catalysts for ORR and

Received: April 24, 2023
Revised: May 10, 2023
Published: May 31, 2023

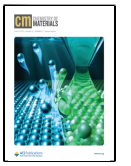

https://doi.org/10.1021/acs.chemmater.3c00970
Chem. Mater. 2023, 35, 4572−4580

OER.[24,25] However, many of these systems are a combination of Ir with other metals,[26−29] and few studies have focused on empty Ir nanoshells. For multimetallic nanocatalysts, dynamical restructuring effects can be problematic and cause the rapid deactivation of the catalyst.[30−32] Some analyses have focused on core−shell designs,[6] but have not investigated Ir nanoshells with an empty core. Additionally, the effects of surface area optimization and structural changes in harsh conditions have not been extensively discussed. Our previous publication has reported the synthesis of core−shell particles with a Cu core and a shell of a platinum-group metal (PGM).[33] The Cu core can be etched by exposure to an oxidative environment, which causes the oxidation and migration of Cu through the Kirkendall effect.[34,35] By removing the Cu core, empty Ir nanoshells are obtained, with a controlled thickness. This work presents the electrochemical properties of core−shell $Cu_{0.79}Ir_{0.21}$ and $Cu_{0.88}Ir_{0.12}$ particles for ORR and OER and their derived Ir nanoshells. Also, we performed a detailed *ex situ* and *in situ* scanning transmission electron microscopy (STEM) study to describe the structure and stability of the samples. Ultimately, the goal is to provide detailed information about structural changes in Ir-based nanostructures with a hollow configuration. As shown with *in situ* STEM and *in situ* X-ray absorption spectroscopy (XAS), traces of Cu remain in the Ir shells even after exposure to harsh oxidative environments. The nanoshells were studied under gaseous environments with reductive and oxidative conditions at 1 bar to understand their stability in a harsh environment. Ir shells from $Cu_{0.79}Ir_{0.21}$ were remarkably stable and resisted treatments at 800 °C without collapsing. Ir shells from $Cu_{0.79}Ir_{0.21}$ and $Cu_{0.88}Ir_{0.12}$ were then tested for ORR and OER. Our results showed that $Cu_{0.88}Ir_{0.12}$ had the highest activity per gram of Ir as the exposed surface of Ir was maximized. However, the stability was not optimal. In contrast, $Cu_{0.79}Ir_{0.21}$ showed high activity and high stability after many electrochemical cycles. Both samples outperformed commercially available Pt particles with a smaller size, as the empty shell structure had a maximized surface area.

MATERIALS AND METHODS

Synthesis of Cu−Ir Particles and Removal of the Cu Core. The $Cu_{0.79}Ir_{0.21}$ and $Cu_{0.88}Ir_{0.12}$ particles were synthesized using a method previously published by our team.[33] All chemicals were purchased from Sigma-Aldrich. For $Cu_{0.79}Ir_{0.21}$, Cu acetate ($Cu(CO_2CH_3)_2$, ≥98% purity) and Ir acetylacetonate ($Ir(acac)_3$, ≥97% purity) were used as precursors. Diphenyl ether (≥99% purity) was used as a solvent and oleylamine (OLAM, ≥70% purity) was used as a capping agent. 20 mg of $Cu(CO_2CH_3)_2$ and 14.3 mg of $Ir(acac)_3$ were dissolved in 20 mL of diphenyl ether and 25 mL of oleylamine in a 100 mL flask. The solution was then heated to 100 °C under <1.0 Torr vacuum with a Schlenk line for 1 h, to remove traces of water. The mixture was then put under a N_2 atmosphere, and the temperature was elevated to 275 °C and maintained for 50 min. The ramp rate was held at 20 °C/min, and the solution was under constant stirring. Increasing the ramp rate will decrease the average nanoparticles diameter. The nucleation of particles causes a change of color as the solution becomes black. It is then cooled down to 40 °C. Hexane is added to the mixture to reduce the viscosity, and it is then centrifuged for 5 min at 8000 rpm. The particles are then deposited at the bottom of the tube. Usually, no antisolvent was necessary as the particles were relatively large and heavy, so they could be easily separated from the rest of the solution. If necessary, ethanol could be added before centrifugation to improve the separation. The particles are then redispersed in hexane and deposited on Vulcan carbon black. Ligands are removed with plasma cleaning with Ar for 30 min followed by calcination under air at 500 °C for 2 min.[36] The calcination causes the rapid oxidation of the Cu core, which migrates outside of the shell and leaves an empty shell of Ir on the carbon support. Masses of Cu oxide could be detected on the support and are the result of the migration and aggregation of Cu oxide during the calcination. The synthesis and processing of $Cu_{0.88}Ir_{0.12}$ is similar to the above procedure for $Cu_{0.79}Ir_{0.21}$. The only difference is the quantity of precursor (7.4 mg of Ir acetylacetonate and 20 mg of Cu acetate). The quantities of diphenyl ether and oleylamine are the same as for $Cu_{0.79}Ir_{0.21}$. For $Cu_{0.79}Ir_{0.21}$ particles, the Ir shell was thicker than the one obtained with $Cu_{0.88}Ir_{0.12}$. Indeed, increasing the amount of Ir makes the Ir shell larger. Thus, this recipe allows to control over the thickness of the core−shell structure and the derived Ir nanoshells.

Scanning Transmission Electron Microscopy. All samples were analyzed with a JEOL NEOARM operating at 200 kV. For STEM imaging, the probe current was set to 150 pA, with a condenser lens aperture of 40 μm and a camera length of 4 cm. Energy-dispersive X-ray spectroscopy (EDS) and electron energy-loss spectroscopy (EELS) were also performed with a probe current of 500 pA, a condenser lens aperture of 40 μm, and a camera length of 2 cm. For *ex situ* analysis, the samples supported on amorphous carbon were diluted in isopropanol, and a drop of the solution was deposited on a nickel-based TEM grid with lacey carbon (purchased from EMS). *In situ* diagnostics were performed with a gas-heating holder for environmental studies provided by Hummingbird Scientific. Gases with ultrahigh purity (99.999%) were used with a mass flow of 5 sccm. All experiments were performed at 1 bar. The delivery of gases was performed with a mass flow control system provided by Hummingbird Scientific.[37,38] For *in situ* EDS, the holder was slightly tilted in the column of the microscopy to optimize the detection of fluorescent X-rays by the two EDS detectors (provided by JEOL USA, Inc.) above the holder. The gas lines were purged with N_2 before the insertion of active gases (O_2 or H_2). STEM images, EDS, and EELS data were processed with DigitalMicrograph, a software provided by Gatan, Inc. EELS data were acquired with a K2 summit camera, also provided by Gatan, Inc.

X-ray Absorption Spectroscopy. *In situ* XAS was performed at the microXAS beamline (X05LA) at the Swiss Light Source (SLS) of the Paul Scherrer Institute (PSI). Data for Cu K and Ir L_2 edge was collected in fluorescence mode, with Silicon Drift detectors. Ir L_3 could not be analyzed due to the presence of W in the sample holder. Hence, the W L_2 overlapped with the Ir L_3 edge. The flux was 2×10^{12} ph/s/400 mA, and the spot size was approximately 10×10 μm^2. The sample was enclosed in the same environmental holder used for *in situ* STEM, with the same flow rates, gases, and temperatures. All experiments were performed at 1 bar. All data were analyzed with Athena and Artemis of the Demeter package.[39]

Electrochemical Analysis. All samples were supported on amorphous carbon. Electrochemical measurements were performed using standard protocols. Data was collected on a potentiostat (Epsilon, Bioanalytical Systems, Inc.) with a three-electrode system consisting of a glassy carbon working electrode (6 mm diameter), a Ag/AgCl reference electrode in 3 M KCl, and a Pt coil auxiliary electrode. The reaction took place in a one-compartment cell. All potentials collected during the testing were converted in reference to a reversible hydrogen electrode (RHE). The catalyst ink was formed through sonication of water, isopropanol, and Nafion at a volume ratio of 4:1:0.01 and an NC on carbon concentration of 2 mg/mL. 10 μL of ink was deposited onto the working electrode at 100 rpm and dried under 700 rpm rotation. For Ir nanoshells on carbon, the weight loading of Ir was 10%. For the commercial Pt catalyst (supported on carbon), the weight loading of Pt was 20%. For aqueous environments, cyclic voltammetry (CV) was taken in a range of 0.0−1.0 V *vs* RHE for ORR and 1.2−1.7 V *vs* RHE for OER at a scan rate of 50 mV/s in N_2 saturated 0.1 M $HClO_4$. For alkaline environments, a 0.1 M KOH solution was used, and the CV was performed in a range of −0.4 to 0.5 V *vs* RHE for ORR and 0.7 to 1.2 V for OER. To test for stability, the samples were cycled between 0.6 and 1.0 V *vs* RHE in N_2 saturated 0.1 M $HClO_4$, with cyclic voltammetry (CV) curves taken

https://doi.org/10.1021/acs.chemmater.3c00970
Chem. Mater. 2023, 35, 4572−4580

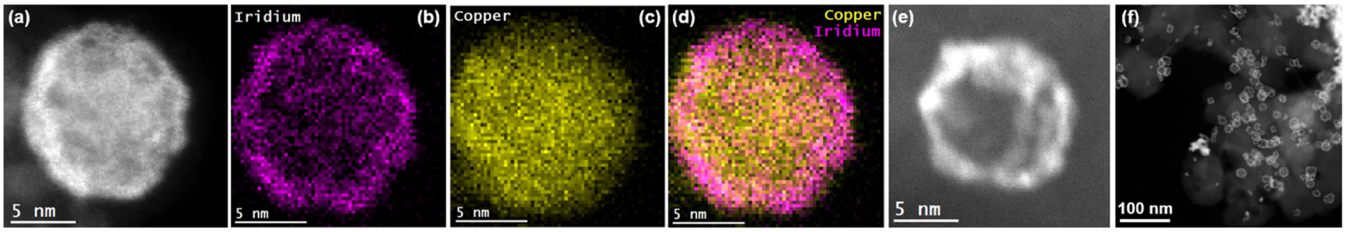

Figure 1. Representative HAADF-STEM and EDS data of the sample studied in this work. (a) HAADF-STEM image of a freshly synthesized $Cu_{0.79}Ir_{0.21}$ particles with a core−shell configuration. (b) EDS map for Ir. (c) EDS map for Cu. (d) Combined EDS data. (e) Empty shell of another particle after calcination. The void left by the copper after oxidation is clearly visible. (f) Large area showing empty Ir shells on C support.

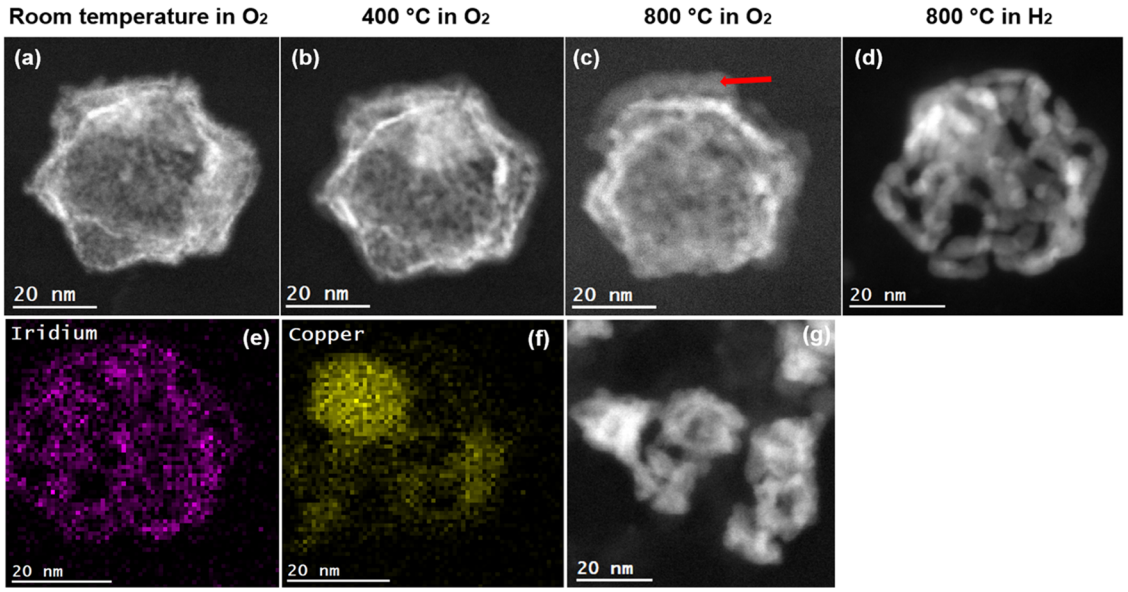

Figure 2. *In situ* STEM analysis of a $Cu_{0.79}Ir_{0.21}$ particles with 1 bar of gases. (a) Fresh sample. Oxidation in air caused some removal of the Cu core. (b) After 30 min exposure to O_2 at 400 °C. (c) After 30 min exposure to O_2 at 800 °C. The red arrow indicates Cu oxide, on top of the Ir shell. (d) After 20 min exposure to H_2 to reduce the Cu and make the Ir shell more visible. (e, f) Corresponding EDS maps to the image in (d). (g) Other particles after the same treatment. The spherical shape was maintained and did not collapse after the treatment.

after 50 cycles at the beginning-of-life (BOL), 5000, 10 000, and 25 000 cycles. The electrochemically active surface area (ECSA) was determined using hydrogen underpotential deposition measurements.[38] Linear sweep voltammetry (LSV) was taken at 1600 rpm from 0.0 to 1.0 V *vs* RHE. IR compensation was performed using the automatic feature of the potentiostat. The mass activity was normalized by Ir mass determined from ICP-OES, and the specific activity was normalized by ECSA.[40]

RESULTS AND DISCUSSION

The synthesis of $Cu_{0.79}Ir_{0.21}$ (Cu/Ir atomic ratio of 79:21) and $Cu_{0.88}Ir_{0.12}$ (Cu/Ir atomic ratio of 88:12) provides core−shell particles with Ir on the surface and Cu in the core, as described in our previous work.[33] The Ir shell will be thicker if more $Ir(acac)_3$ is added to the mixture. Hence, there is a tunable control over the Ir shell's thickness which can be beneficial to optimize the surface area of exposed Ir. Figure 1 provides high-angle annular dark-field (HAADF-STEM) images of a $Cu_{0.79}Ir_{0.21}$ particle with EDS data showing the core−shell structure. It is possible to see some Cu coming out of the Ir shell as it is lightly oxidized after air exposure. Electron energy-loss spectroscopy (EELS) data are provided in Figure S1 and are consistent with a mixture of Cu(0) and Cu(II). The oxidation of Cu causes migration of Cu from the core to the outside through the Kirkendall effect and has been documented in previous studies on Cu particles.[41] When the sample is calcinated at 500 °C, Cu quickly oxidizes and leaves an empty shell of Ir, as seen in Figure 1e. Some traces of Cu can be detected in empty shells, as provided in Figure S2. Low-magnification STEM images showing many particles before and after oxidation are provided in Figure S3. The diameter of 200 $Cu_{0.79}Ir_{0.21}$ nanoparticles was measured and showed that the average diameter was 13.8 nm with a standard deviation of 1.7 nm. The particles shown in Figure 1 are representative examples of the overall system, as the Ir shells' thickness and their diameters were similar for many particles.

To better understand the stability of the Ir shells in harsh environments, an *in situ* STEM analysis was performed on as-synthesized samples. It was not possible to perform *in situ* experiments in a liquid environment (as for ORR and OER) with high-resolution images and spectroscopic data. Hence, we used hot gases (O_2 and H_2 at elevated temperatures) to mimic harsh conditions that could happen in liquid phases. Additionally, the *in situ* experiment in gases provides information about changes that could be expected under extreme conditions for a wider range of catalytic processes. Since the imaging resolution is slightly lower with *in situ* configuration, we selected a large $Cu_{0.79}Ir_{0.21}$ particle and tracked changes in its morphology during exposure to oxygen at 1 bar and with increased temperature. Results are summarized in Figure 2. Initially, some Cu was oxidized due

https://doi.org/10.1021/acs.chemmater.3c00970
Chem. Mater. 2023, 35, 4572−4580

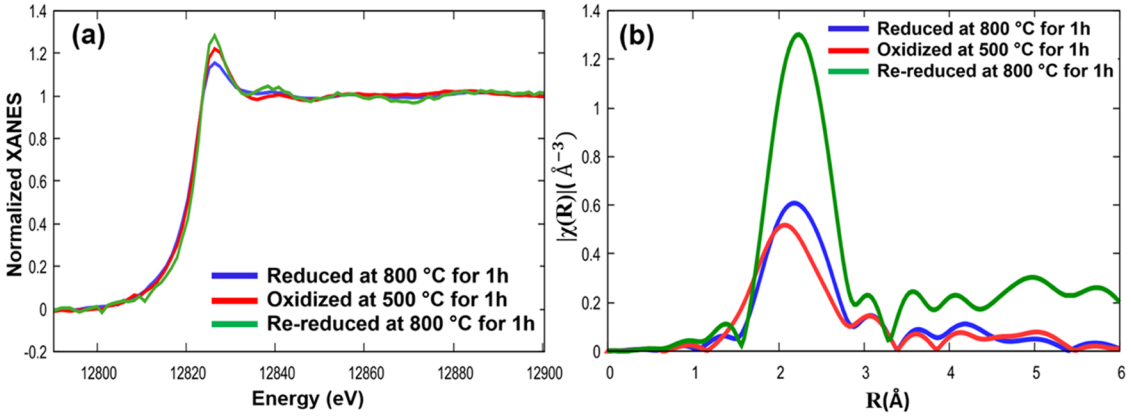

Figure 3. Measurements of Ir L_2 edge with *in situ* XAS analysis under gaseous environments. (a) XANES data and (b) FT-EXAFS. The main peak corresponds to Ir−Ir bonds.

Table 1. Summary of EXAFS Fitting of the $Cu_{0.79}Ir_{0.21}$ Particles after Oxidation and Reduction[a]

sample	N_{Ir-Ir}	N_{Ir-Cu}	N_{Ir-O}	d_{Ir-Ir} (Å)	d_{Ir-Cu} (Å)	d_{Ir-O} (Å)
$Cu_{0.79}Ir_{0.21}$ after reduction at 800 °C	5.0 ± 3.0	8.9 ± 4.2		2.58 ± 0.15	2.62 ± 0.08	
$Cu_{0.79}Ir_{0.21}$ after oxidation at 500 °C (Ir shell)	3.6 ± 1.4	1.1 ± 0.6	0.6 ± 0.8	2.65 ± 0.02	2.65 ± 0.04	1.98 ± 0.04
$Cu_{0.79}Ir_{0.21}$ after re-reduction at 800 °C (Ir shell)	5.8 ± 2.2	5.4 ± 1.7		2.66 ± 0.03	2.61 ± 0.02	

[a]A comparison of the experimental data and the fits in R-space is provided in Figure S7.

to exposure to air. We see that the increase in temperature under O_2 causes further oxidation and migration of remaining Cu that accumulates on the surface of the shell. The oxidized Cu can be seen on top of the Ir shell in Figure 2c, as indicated by the red arrow. The dull halo corresponds to dispersed Cu oxide, whereas bright regions correspond to Ir, which is heavy. In HAADF-STEM mode, the brightness of elements is proportional to $Z^{1.6}$; hence, the Cu oxide can be easily distinguished from Ir.[42] One can also notice the coarsening of the Ir shell, which is particularly visible after the gas was switched to H_2. This causes the reduction of Cu and a decrease in volume, which makes the Ir shell more visible. We see that after a harsh treatment, some coarsening occurred, but no collapse of the shell happened. Hence, the Ir shells are extremely stable at high temperatures, making them excellent candidates for sustainable catalysis. Some holes in the shell can be identified in the STEM image in Figure 2d as well as in the corresponding EDS maps in Figure 2e,f. Other shells did not have many holes and remained spherical with some coarsening, as seen in Figure 2g. Additional EDS maps are provided in Figure S4 and show similar results to those provided in Figure 2: Residual Cu oxide was detected even after strong oxidation conditions. Hence, Cu cannot fully migrate toward the outside of the Ir shell and should be factored in when electrochemical properties are measured. Finally, the same experiment (reduction and oxidation) was performed on thinner Ir shells derived from $Cu_{0.88}Ir_{0.12}$ particles. In that case, the nanoshell architecture collapsed and coarsening occurred (Figure S5).

To expand and complete the analysis performed with *in situ* STEM, we also performed *in situ* XAS experiments. The two purposes of doing *in situ* XAS were as follows: First, the desire for a global analysis of a large quantity of particles: The beam size of STEM does not allow us to investigate large regions, whereas XAS is an ensemble-average method that provides results for all nanoparticles. The second reason is to determine the mixing of remaining Cu after oxidation treatment and detect potential alloying or segregation of Cu and Ir that could influence catalytic properties. In fact, alloying and strong interactions between Ir and Cu atoms will modulate adsorption and desorption energies of molecules, ultimately impacting the activity of the catalyst. *In situ* XAS analysis was performed on the core−shell sample after reduction, oxidation, and re-reduction, with additional details provided in the Supporting Information (Tables S1 and S2). After oxidation, Cu is removed from the core through the Kirkendall effect as seen in the STEM analysis. We exposed the sample to reductive and oxidative conditions at elevated temperatures to detect if Cu and Ir form an alloyed phase under certain environmental conditions: This will help us to better understand catalytic properties when the samples are tested for ORR and OER, which are oxidative and reductive environments, respectively. The measurements for the Ir L_2 edge are summarized in Figure 3. In Figure 3a, the X-ray absorption near-edge structure (XANES) spectra are provided after various redox conditions at 1 bar, with O_2 and H_2. The Fourier transform of the extended X-ray absorption fine structure (EXAFS) spectra is provided in Figure 3b.

Based on the XANES data of the Ir L_2 edge, no striking difference can be seen after oxidation or re-reduction. The analysis of the FT-EXAFS data shows a small shift of the main peak to lower *R* values (red plot with a peak at 2.0 Å), indicating the possibility of shorter bonds, such as Ir−O. This is consistent with the harsh oxidative conditions. After re-reduction (green plot), the main peak is slightly shifted to larger *R* values (peak at 2.2 Å) and overlaps well with the data for the initially reduced core−shell particles (blue plot).

The EXAFS data were fitted with models to determine the coordination number (*N*) and distances (*d*) of Ir−Ir bonds, Ir−Cu bonds, and Ir−O bonds (Table 1). First, the coordination numbers for Ir−Ir and Ir−Cu bonds for the reduced core−shell structure are consistent with the morphology of the sample. The Ir shell does not really mix with the Cu core at high annealing temperatures (as seen with *in situ* STEM-EDS data provided in Figure S6). Thus, a

https://doi.org/10.1021/acs.chemmater.3c00970
Chem. Mater. 2023, 35, 4572−4580

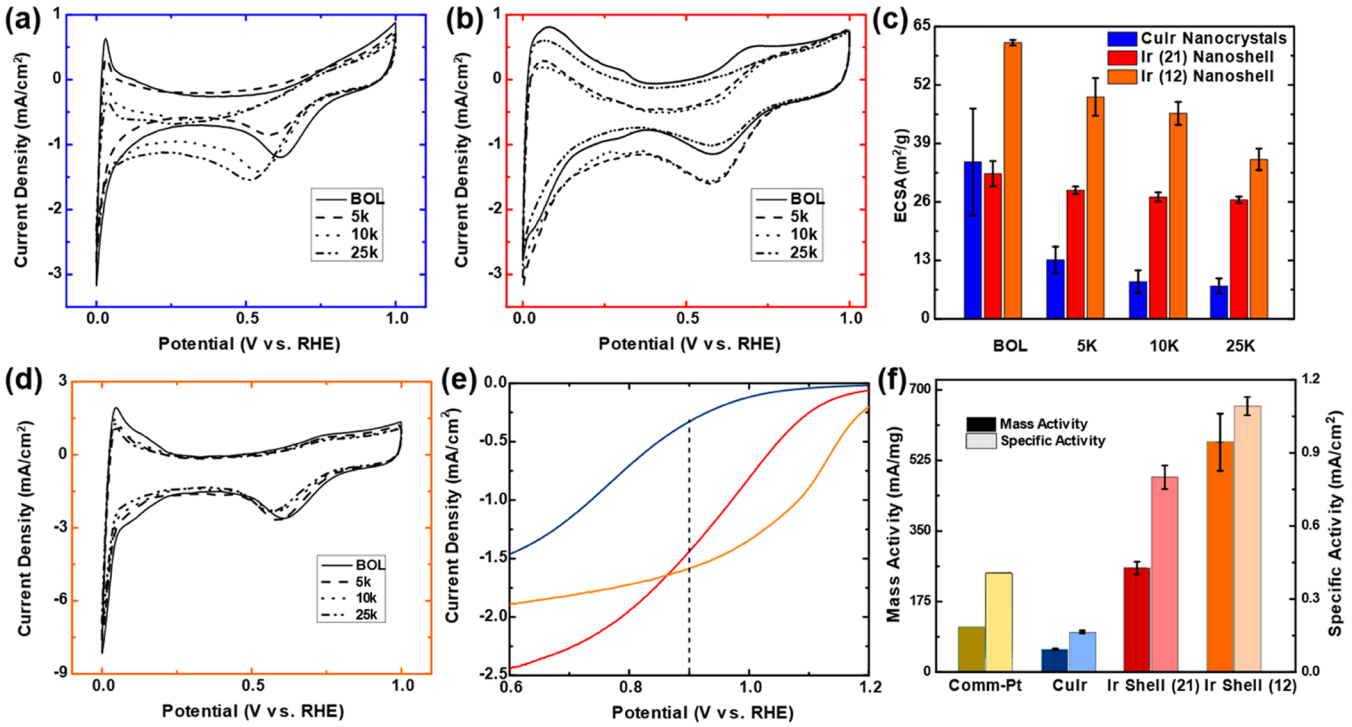

Figure 4. Electrochemical measurements for ORR in acidic medium. (a–c) CV curves for CuIr, $Cu_{0.79}Ir_{0.21}$, and $Cu_{0.88}Ir_{0.12}$ particles, respectively, at BOL and after 5000, 10 000, and 25 000 redox cycles. (d) LSV curves for the same samples. (e) Stability data for these samples after the same cycling parameters. (f) Mass and specific activities for the same samples, including commercial Pt in yellow. Kinetic current densities were extracted at 0.9 V *vs* RHE.

coordination number for N_{Ir-Ir} of 5 is consistent with an Ir shell on a Cu core. However, N_{Ir-Cu} is a bit high, so one can speculate that a small quantity of Cu atoms are mixed with Ir. Even though Ir and Cu are not known to be miscible, previous reports have underlined the miscibility of Ir and Cu at the nanoscale.[43] After oxidation, N_{Ir-Ir} and N_{Ir-Cu} drop due to the change in morphology. Indeed, the drop of N_{Ir-Cu} can be caused by the removal of the Cu core or by the oxidation of Ir (with the formation of Ir–O bonds instead of Cu–Ir bonds). However, the drop of N_{Ir-Cu} is much more substantial than the drop of N_{Ir-Ir}, which indicates that oxidation of Ir is not fully responsible for the decrease of N_{Ir-Cu}. In fact

$$\frac{(N_{Ir-Cu})_{red}}{(N_{Ir-Ir})_{red}} > \frac{(N_{Ir-Cu})_{ox}}{(N_{Ir-Ir})_{ox}}$$

Thus, the strong drop in Ir–Cu bonds indicates a substantial removal of Cu atoms during oxidation, although some traces of Cu remain in the Ir shells. The drop in N_{Ir-Ir} is due to the partial oxidation of Ir, which diminishes the number of metal–metal bonds. Finally, the sample was re-reduced, and EXAFS data shows that N_{Ir-Cu} and N_{Ir-Ir} increased again. One can conclude that the presence of remaining Cu is not negligible as it stays close to 5.4. For all three steps (reduced, oxidized, or re-reduced), one can notice that d_{Ir-Ir} is lower than the bond distance of pure Ir (2.74 Å). One can speculate that some Cu atoms are inserted into the lattice of the Ir nanoshells, creating some distortions which may shorten the Ir–Ir bonds. For d_{Ir-Cu}, the distance remains between 2.61 and 2.65 Å, which is between the bond distance of pure Cu (2.54 Å) and pure Ir (2.74 Å). Based on the values of bond lengths and coordination numbers, there is no indication of an alloyed phase at any step of the experiment, which is consistent with the known immiscibility of Ir and Cu. Thus, even though some Cu atoms may be inserted into the Ir phase, we did not observe the formation of a substantial alloyed phase. To summarize, Cu atoms remain after the oxidation or re-reduction of the sample and still interact with Ir atoms in the nanoshells.

Finally, XANES data for Cu are provided in Figure S8 and show the clear oxidation of Cu after exposure to O_2 and subsequent re-reduction after exposure to H_2. As shown by *in situ* STEM data, Cu migrates outside of the Ir shells and coalesces in large masses of Cu oxide (Figure S9).

Following the full characterization of the sample, we tested $Cu_{0.79}Ir_{0.21}$ and $Cu_{0.88}Ir_{0.12}$ particles for their electrochemical performance. ORR and OER were investigated. The free-standing particles were deposited on amorphous carbon, and the sample was plasma-cleaned with Ar and calcinated at 500 °C in air for 2 min, causing the removal of the Cu core and leaving empty shells of Ir. We also tested core–shell Cu–Ir particles without the removal of the core to understand the impact of Cu removal. In that case, the samples were plasma-cleaned with Ar for 40 min without calcination to prevent oxidation.

The samples are first tested in acidic medium for ORR, and results are shown in Figure 4. The CV curves of core–shell $Cu_{0.79}Ir_{0.21}$ particles and Ir shells from both $Cu_{0.79}Ir_{0.21}$ and $Cu_{0.88}Ir_{0.12}$ are shown in Figure 4a–c. Measurements were performed on fresh particles after 50 initial cycles (beginning of life = BOL), after 5000, 10 000, and 25 000 cycles. The ECSA of the three samples is provided in Figure 4e and shows that at 61.42 ± 0.60 m^2/g, the thin Ir shell derived from $Cu_{0.88}Ir_{0.12}$ particles have a higher ECSA than Ir shells derived from $Cu_{0.79}Ir_{0.21}$, at 32.28 ± 2.79 m^2/g, or core–shell $Cu_{0.79}Ir_{0.21}$, at 34.88 ± 11.88 m^2/g. This makes sense, as the

https://doi.org/10.1021/acs.chemmater.3c00970
Chem. Mater. 2023, 35, 4572–4580

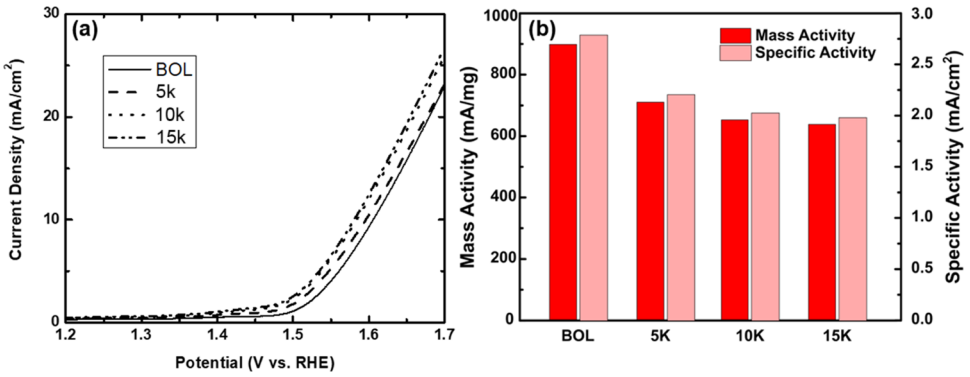

Figure 5. Ir shells from $Cu_{0.79}Ir_{0.21}$ particles tested for OER in acidic medium. (a) *I*−*V* curve. (b) Mass activity and specific activity after cycling. Kinetic current densities were extracted at 1.53 V *vs* RHE.

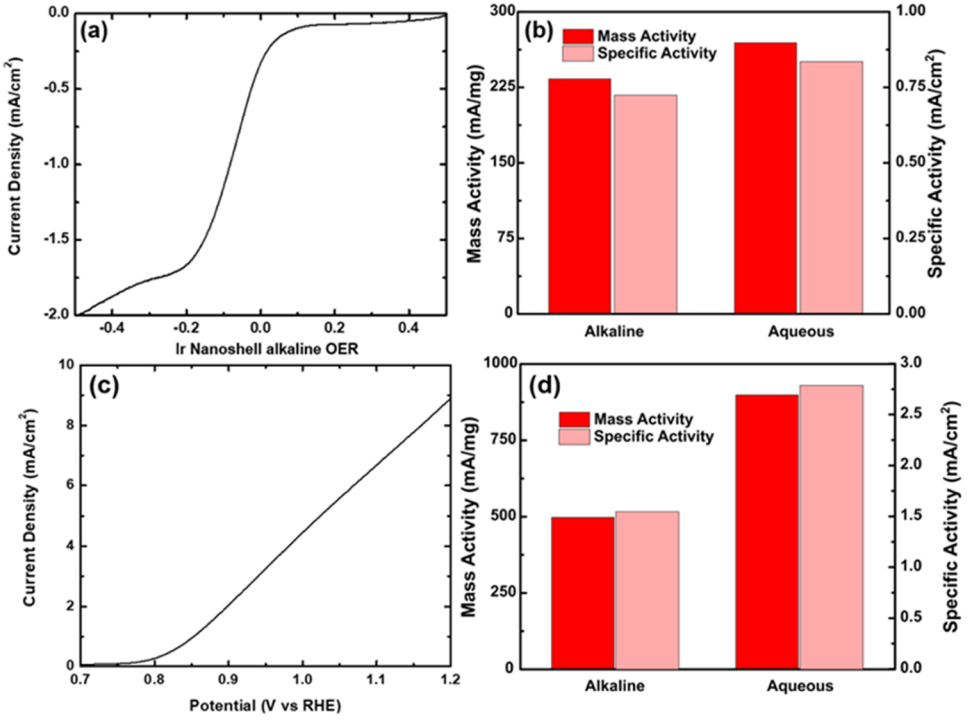

Figure 6. Results of ORR and OER testing of thick Ir shells in an alkaline environment. The results are then compared to those obtained for acidic (aqueous) conditions. (a) LSV curve for the sample tested for ORR in alkaline medium. (b) Comparison of the mass and specific activity in alkaline and acidic (aqueous) medium for ORR. (c) *I*−*V* curve for the sample tested for OER in alkaline medium. (d) Comparison of the mass and specific activity in alkaline and acidic (aqueous) medium, when OER was investigated.

reduction in thickness allows for greater atomic optimization of the Ir by limiting the number of sub-surface atoms. At the BOL, these Ir shells were clearly the more performant sample. However, one could notice a strong drop in ECSA after cycling, lowering to 35.45 ± 2.40 m^2/g, or nearly 42.28% after 25 000 cycles. In contrast, Ir shells from $Cu_{0.79}Ir_{0.21}$ have a lower surface area at BOL but are more stable after many cycles, decreasing to only 26.46 ± 0.72 m^2/g, or 18.03% after 25 000 cycles. This underlines the subtle balance between surface optimization and stability and is well in line with our results from *in situ* STEM. The robust thick Ir shells were not damaged during cycling and retained most of their ECSA. Also, Figure 4f shows that both of the Ir shell samples outperformed commercial Pt samples (3 nm Pt particles supported on carbon with a 20 wt % metallic loading) in terms of mass activity and specific activity. The commercial Pt catalyst showed a mass activity of approximately 112.42 mA/mg, and a specific activity of 0.40 mA/mg, which is in excellent agreement with previous reports.[2,44] In comparison, the thin Ir shells showed a mass activity of 568.03 ± 70.37 mA/mg and a specific activity of 1.76 ± 0.22 mA/cm^2, indicating the Ir shells are capable of mass activity approximately 80.21% greater than commercial Pt, and a specific activity approximately 77.27% greater than commercial Pt. This high activity is a direct consequence of the design of the shell. In contrast, core−shell $Cu_{0.79}Ir_{0.21}$ were less active at 95.94 ± 0.98 mA/mg and 0.28 ± 0.00 mA/cm^2, and had poor stability, decreasing 79.01% after 25 000 cycles. This is due to the Cu core that can passivate the Ir surface and also oxidize slowly, ultimately covering the surface. For both Ir shell samples, one could expect that the traces of remaining Cu may slightly passivate the Ir atoms as Cu has lower catalytic properties for ORR and OER than Ir.[45−48] Cu may also play a role in the deactivation of the very thin shells, possibly through dynamical restructuring effects during cycling.

https://doi.org/10.1021/acs.chemmater.3c00970
Chem. Mater. 2023, 35, 4572−4580

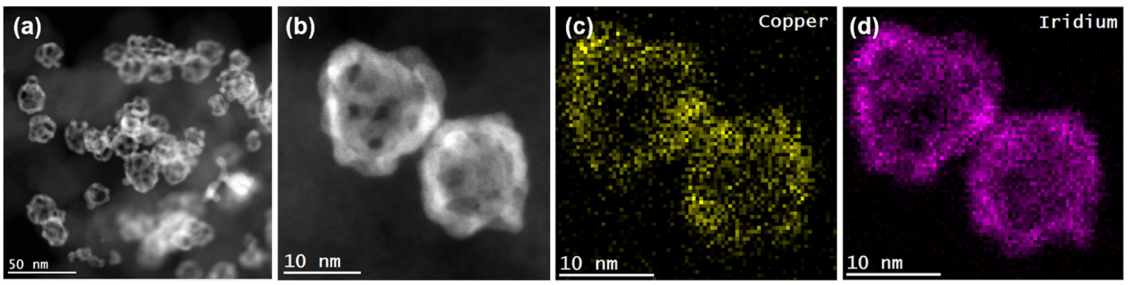

Figure 7. STEM analysis of Ir shells (derived from $Cu_{0.79}Ir_{0.21}$ particles) after 25 000 cycles of testing for ORR in an acidic medium. (a) Low-magnification HAADF-STEM image. (b) High-magnification HAADF-STEM image. (c) EDS map for Cu of the particles shown in (b). (d) EDS map for Ir of the particles shown in (b).

Since the thick Ir shells that were derived from $Cu_{0.79}Ir_{0.21}$ particles are more stable, and hence a better catalyst for long-term use, we decided to pursue the investigation for OER in an acidic environment. Figure 5 shows the stability of the sample for OER, which is similar to what we observed for ORR, only decreasing in mass activity by approximately 28.99% from 898.69 to 638.17 mA/mg after 15 000 cycles. Thus, the mass activity and specific activity (Figure 5b) remain high at the beginning and at the end of the cycling, up to 15 000 cycles. The thick Ir shells have superior catalytic activity and stability compared to other commonly used catalysts for OER.

Based on the excellent activities and stability of the thick Ir shells for both ORR and OER in acidic conditions, we now check to see the catalyst performance in alkaline medium. The alkaline performance of the thick Ir shells was tested and compared to that under acidic or aqueous conditions. Results for testing in alkaline conditions are summarized in Figure 6 and show high mass and specific activities for both reactions. In fact, in alkaline medium for ORR as seen in Figure 6a,b, thick Ir shells show a mass activity of approximately 233.432 mA/mg, and a specific activity of 0.72 mA/cm^2, decreasing only 13.29% from its performance in aqueous environments. Similarly, the OER performance of the thicker Ir shells in alkaline medium shows a mass activity of 498.71 mA/mg and a specific activity of 1.54 mA/cm^2. This OER performance as seen in Figure 6c,d decreases slightly more significantly from the performance in aqueous environment, by approximately 44.62%. This is an advantage of Ir over Pt and over common catalysts for ORR and OER, which tend to be efficient for only one medium (acidic or alkaline).[25,49−51] Thus, we designed a stable catalyst that shows promising properties for ORR and ORR in alkaline and in acidic environments. The ability to have a highly active catalyst for both ORR and OER in both aqueous and alkaline conditions is a major advancement toward universal catalysts for fuel cell applications.

One should notice that residual Cu in the sample plays a minor role in the catalytic properties of the sample. Cu particles were synthesized using a previously reported method,[33] and the particles were tested for ORR and OER in acidic environments. The results are provided in Figure S10 and show minimal activity compared to the Ir-based samples.

Finally, we performed a STEM investigation of the particles after 25 000 cycles for ORR in acidic environments to corroborate the stability experiments performed electrochemically in aqueous solution. The results are shown in Figure 7 and explain the stability of the catalytic performances: In fact, the shells are slightly coarsened but did not collapse, which explains the excellent stability observed with ORR measurements. This is not surprising as the *in situ* STEM analysis under harsh conditions proved the excellent stability of the thick Ir shells.

CONCLUSIONS

To summarize, we performed a detailed characterization of Ir shells obtained after the oxidation of Cu−Ir core−shell particles. We demonstrated that Ir shells are extremely robust structures, especially if they are thick enough. *In situ* STEM analysis combined with *in situ* XAS analysis showed that some traces of Cu remained in the Ir shells, although no substantial mixing between Cu and Ir was detected. Catalytic testing for ORR and OER in acidic and alkaline environments showed promising mass and specific activity for thin and thick Ir shells, both outperforming commercially available samples. The thick Ir shells were highly stable, due to the robustness of the structure as seen by STEM analysis. This work provides an innovative design for Ir-based catalysts and shows that stability and enhanced activity can be both achieved. We hope this analysis will expand the range of available nanostructures to perform sustainable, low-cost, and efficient catalytic processes.

ASSOCIATED CONTENT

Supporting Information

The Supporting Information is available free of charge at https://pubs.acs.org/doi/10.1021/acs.chemmater.3c00970.

Additional STEM and TEM images, EELS and EDS data; and ORR and OER data (PDF)

AUTHOR INFORMATION

Corresponding Authors

Christopher B. Murray − *Department of Materials Science and Engineering, University of Pennsylvania, Philadelphia, Pennsylvania 19104, United States; Department of Chemistry, University of Pennsylvania, Philadelphia, Pennsylvania 19104, United States*; Email: cbmurray@sas.upenn.edu

Eric A. Stach − *Department of Materials Science and Engineering, University of Pennsylvania, Philadelphia, Pennsylvania 19104, United States; Laboratory for Research on the Structure of Matter, University of Pennsylvania, Philadelphia, Pennsylvania 19104, United States;* orcid.org/0000-0002-3366-2153; Email: stach@seas.upenn.edu

Authors

Alexandre C. Foucher − *Department of Materials Science and Engineering, University of Pennsylvania, Philadelphia,*

https://doi.org/10.1021/acs.chemmater.3c00970
Chem. Mater. 2023, 35, 4572−4580

Pennsylvania 19104, United States; orcid.org/0000-0001-5042-4002

Daniel J. Rosen − *Department of Materials Science and Engineering, University of Pennsylvania, Philadelphia, Pennsylvania 19104, United States;* orcid.org/0000-0003-1463-7363

Shengsong Yang − *Department of Chemistry, University of Pennsylvania, Philadelphia, Pennsylvania 19104, United States*

Dario Ferreira Sanchez − *Paul Scherrer Institute, 5232 Villigen, Switzerland*

Ilia Sadykov − *Paul Scherrer Institute, 5232 Villigen, Switzerland*

Daniel Grolimund − *Paul Scherrer Institute, 5232 Villigen, Switzerland;* orcid.org/0000-0001-9721-7940

Anatoly I. Frenkel − *Department of Materials Science and Chemical Engineering, Stony Brook University, Stony Brook, New York 11794, United States; Division of Chemistry, Brookhaven National Laboratory, Upton, New York 11973, United States;* orcid.org/0000-0002-5451-1207

Complete contact information is available at: https://pubs.acs.org/10.1021/acs.chemmater.3c00970

Author Contributions

[▽]A.C.F. and D.J.R. contributed equally to this work.

Notes

The authors declare the following competing financial interest(s): One of the authors (E.A.S.) has an equity interest in Hummingbird Scientific.

■ ACKNOWLEDGMENTS

This work was primarily supported as part of the Integrated Mesoscale Architectures for Sustainable Catalysis (IMASC), an Energy Frontier Research Center funded by the U.S. Department of Energy, Office of Science, Basic Energy Sciences under Award #DE-SC0012573. This work was carried out in part at the Singh Center for Nanotechnology, which is supported by the NSF National Nanotechnology Coordinated Infrastructure Program under grant NNCI-2025608. Additional support to the Nanoscale Characterization Facility at the Singh Center has been provided by the Laboratory for Research on the Structure of Matter (MRSEC) supported by the National Science Foundation (DMR-1720530). The Swiss Light Source at Paul Scherrer Institute, Villigen, Switzerland, is acknowledged for beamline time at the microXAS beamline (X05LA). The authors appreciate useful discussions with Drs. O. Safonova and M. Nachtegaal. They also thank Dr. Chang Liu (University of Pennsylvania) for the control experiment shown in Figure S10.

■ REFERENCES

(1) Bartholomew, C. H.; Farrauto, R. J.*Fundamentals of Industrial Catalytic Processes*, 2nd ed.; John Wiley & Sons, Inc., 2010; pp 1−966.

(2) Rosen, D. J.; Foucher, A. C.; Lee, J. D.; Yang, S.; Marino, E.; Stach, E. A.; Murray, C. B. Microwave Heating of Nanocrystals for Rapid, Low-Aggregation Intermetallic Phase Transformations. *ACS Mater. Lett.* **2022**, *4*, 823−830.

(3) Jia, Q.; Caldwell, K.; Strickland, K.; Ziegelbauer, J. M.; Liu, Z.; Yu, Z.; Ramaker, D. E.; Mukerjee, S. Improved Oxygen Reduction Activity and Durability of Dealloyed PtCox Catalysts for Proton Exchange Membrane Fuel Cells: Strain, Ligand, and Particle Size Effects. *ACS Catal.* **2015**, *5*, 176−186.

(4) Shao, M.; Chang, Q.; Dodelet, J.-P.; Chenitz, R. Recent Advances in Electrocatalysts for Oxygen Reduction Reaction. *Chem. Rev.* **2016**, *116*, 3594−3657.

(5) Xiao, M.; Zhu, J.; Li, G.; Li, N.; Li, S.; Cano, Z. P.; Ma, L.; Cui, P.; Xu, P.; Jiang, G.; Jin, H.; Wang, S.; Wu, T.; Lu, J.; Yu, A.; Su, D.; Chen, Z. A Single-Atom Iridium Heterogeneous Catalyst in Oxygen Reduction Reaction. *Angew. Chem.* **2019**, *131*, 9742−9747.

(6) Nong, H. N.; Gan, L.; Willinger, E.; Teschner, D.; Strasser, P. IrOx Core-Shell Nanocatalysts for Cost- and Energy-Efficient Electrochemical Water Splitting. *Chem. Sci.* **2014**, *5*, 2955−2963.

(7) Inaba, M.; Zana, A.; Quinson, J.; Bizzotto, F.; Dosche, C.; Dworzak, A.; Oezaslan, M.; Simonsen, S. B.; Kuhn, L. T.; Arenz, M. The Oxygen Reduction Reaction on Pt: Why Particle Size and Interparticle Distance Matter. *ACS Catal.* **2021**, *11*, 7144−7153.

(8) Garlyyev, B.; Kratzl, K.; Rück, M.; Michalička, J.; Fichtner, J.; Macak, J. M.; Kratky, T.; Günther, S.; Cokoja, M.; Bandarenka, A. S.; Gagliardi, A.; Fischer, R. A. Optimizing the Size of Platinum Nanoparticles for Enhanced Mass Activity in the Electrochemical Oxygen Reduction Reaction. *Angew. Chem., Int. Ed.* **2019**, *58*, 9596−9600.

(9) Sung, M.; Kim, J. Oxygen Evolution Reaction on Pt Sphere and Ir-Modified Pt Sphere Electrodes with Porous Structures. *Int. J. Hydrogen Energy* **2018**, *43*, 2130−2138.

(10) Reier, T.; Oezaslan, M.; Strasser, P. Electrocatalytic Oxygen Evolution Reaction (OER) on Ru, Ir, and Pt Catalysts: A Comparative Study of Nanoparticles and Bulk Materials. *ACS Catal.* **2012**, *2*, 1765−1772.

(11) Uribe-Godínez, J.; Altamirano-Gutiérrez, A. Systematic Study of Iridium-Based Catalysts Derived from $Ir_4(CO)_{12}$, Capable to Perform the ORR and HOR. *Catal. Today* **2021**, *374*, 124−134.

(12) Huang, B.; Zhao, Y. Iridium-Based Electrocatalysts toward Sustainable Energy Conversion. *EcoMat* **2022**, *4*, No. e12176.

(13) Harris, P. J. F. The Sintering of Platinum Particles in an Alumina-Supported Catalyst: Further Transmission Electron Microscopy Studies. *J. Catal.* **1986**, *97*, 527−542.

(14) Alemany-Molina, G.; Quílez-Bermejo, J.; Navlani-García, M.; Morallón, E.; Cazorla-Amorós, D. Efficient and Cost-Effective ORR Electrocatalysts Based on Low Content Transition Metals Highly Dispersed on C3N4/Super-Activated Carbon Composites. *Carbon* **2022**, *196*, 378−390.

(15) Ouyang, C.; Ni, B.; Sun, Z.; Zhuang, J.; Xiao, H.; Wang, X. Boosting the ORR Performance of Modified Carbon Black via C−O Bonds. *Chem. Sci.* **2019**, *10*, 2118−2123.

(16) Kim, Y. T.; Lopes, P. P.; Park, S. A.; Lee, A. Y.; Lim, J.; Lee, H.; Back, S.; Jung, Y.; Danilovic, N.; Stamenkovic, V.; Erlebacher, J.; Snyder, J.; Markovic, N. M. Balancing Activity, Stability and Conductivity of Nanoporous Core-Shell Iridium/Iridium Oxide Oxygen Evolution Catalysts. *Nat. Commun.* **2017**, *8*, No. 1449.

(17) Wang, Y. C.; Rhéaume, É.; Lesage, F.; Kakkar, A. Synthetic Methodologies to Gold Nanoshells: An Overview. *Molecules* **2018**, *23*, No. 2851.

(18) Edgar, J. A.; Zareie, H. M.; Blaber, M.; Dowd, A.; Cortie, M. B. In *Synthesis of Hollow Gold Nanoparticles and Rings Using Silver Templates*, 2008 International Conference on Nanoscience and Nanotechnology, 2008; pp 36−39.

(19) Wang, J. X.; Inada, H.; Wu, L.; Zhu, Y.; Choi, Y. M.; Liu, P.; Zhou, W. P.; Adzic, R. R. Oxygen Reduction on Well-Defined Core-Shell Nanocatalysts: Particle Size, Facet, and Pt Shell Thickness Effects. *J. Am. Chem. Soc.* **2009**, *131*, 17298−17302.

(20) Hsieh, Y. C.; Zhang, Y.; Su, D.; Volkov, V.; Si, R.; Wu, L.; Zhu, Y.; An, W.; Liu, P.; He, P.; Ye, S.; Adzic, R. R.; Wang, J. X. Ordered Bilayer Ruthenium−Platinum Core-Shell Nanoparticles as Carbon Monoxide-Tolerant Fuel Cell Catalysts. *Nat. Commun.* **2013**, *4*, No. 2466.

(21) Chen, C.; Kang, Y.; Huo, Z.; Zhu, Z.; Huang, W.; Xin, H. L.; Snyder, J. D.; Li, D.; Herron, J. A.; Mavrikakis, M.; Chi, M.; More, K. L.; Li, Y.; Markovic, N. M.; Somorjai, G. A.; Yang, P.; Stamenkovic, V. R. Highly Crystalline Multimetallic Nanoframes with Three-Dimensional Electrocatalytic Surfaces. *Science* **2014**, *343*, 1339−1343.

(22) Mourdikoudis, S.; Liz-Marzán, L. M. Oleylamine in Nanoparticle Synthesis. *Chem. Mater.* **2013**, *25*, 1465−1476.
(23) Ghosh, S.; Manna, L. The Many "Facets" of Halide Ions in the Chemistry of Colloidal Inorganic Nanocrystals. *Chem. Rev.* **2018**, *118*, 7804−7864.
(24) Kim, Y.; Jin, D.; Lee, C.; Lee, Y. Iridium-Copper Oxide Nanotubes Catalyzing PH-Universal Oxygen Evolution Reaction with Highly Improved Activity and Durability via Elemental Substitution. *J. Alloys Compd.* **2022**, *909*, No. 164813.
(25) Antolini, E. Iridium as Catalyst and Cocatalyst for Oxygen Evolution/Reduction in Acidic Polymer Electrolyte Membrane Electrolyzers and Fuel Cells. *ACS Catal.* **2014**, *4*, 1426−1440.
(26) Wang, C.; Sui, Y.; Xu, M.; Liu, C.; Xiao, G.; Zou, B. Synthesis of Ni-Ir Nanocages with Improved Electrocatalytic Performance for the Oxygen Evolution Reaction. *ACS Sustainable Chem. Eng.* **2017**, *5*, 9787−9792.
(27) Yoon, D.; Bang, S.; Park, J.; Kim, J.; Baik, H.; Yang, H.; Lee, K. One Pot Synthesis of Octahedral {111} CuIr Gradient Alloy Nanocrystals with a Cu-Rich Core and an Ir-Rich Surface and Their Usage as Efficient Water Splitting Catalyst. *CrystEngComm* **2015**, *17*, 6843−6847.
(28) Cao, D.; Wang, J.; Zhang, H.; Xu, H.; Cheng, D. Growth of IrCu Nanoislands with Rich IrCu/Ir Interfaces Enables Highly Efficient Overall Water Splitting in Non-Acidic Electrolytes. *Chem. Eng. J.* **2021**, *416*, No. 129128.
(29) Zhu, J.; Chen, Z.; Xie, M.; Lyu, Z.; Chi, M.; Mavrikakis, M.; Jin, W.; Xia, Y. Iridium-Based Cubic Nanocages with 1.1-Nm-Thick Walls: A Highly Efficient and Durable Electrocatalyst for Water Oxidation in an Acidic Medium. *Angew. Chem., Int. Ed.* **2019**, *58*, 7244−7248.
(30) Zugic, B.; Wang, L.; Heine, C.; Zakharov, D. N.; Lechner, B. A. J.; Stach, E. A.; Biener, J.; Salmeron, M.; Madix, R. J.; Friend, C. M. Dynamic Restructuring Drives Catalytic Activity on Nanoporous Gold-Silver Alloy Catalysts. *Nat. Mater.* **2017**, *16*, 558−564.
(31) Marcella, N.; Lim, J. S.; Płonka, A. M.; Yan, G.; Owen, C. J.; van der Hoeven, J. E. S.; Foucher, A. C.; Ngan, H. T.; Torrisi, S. B.; Marinkovic, N. S.; Stach, E. A.; Weaver, J. F.; Aizenberg, J.; Sautet, P.; Kozinsky, B.; Frenkel, A. I. Decoding Reactive Structures in Dilute Alloy Catalysts. *Nat. Commun.* **2022**, *13*, No. 832.
(32) Liu, D.; Li, Y.; Kottwitz, M.; Yan, B.; Yao, S.; Gamalski, A.; Grolimund, D.; Safonova, O. V.; Nachtegaal, M.; Chen, J. G.; Stach, E. A.; Nuzzo, R. G.; Frenkel, A. I. Identifying Dynamic Structural Changes of Active Sites in Pt−Ni Bimetallic Catalysts Using Multimodal Approaches. *ACS Catal.* **2018**, *8*, 4120−4131.
(33) Foucher, A. C.; Yang, S.; Rosen, D. J.; Lee, J. D.; Huang, R.; Jiang, Z.; Barrera, F. G.; Chen, K.; Hollyer, G. G.; Friend, C. M.; Gorte, R. J.; Murray, C. B.; Stach, E. A. Synthesis and Characterization of Core-Shell Cu-Ru, Cu-Rh, and Cu-Ir Nanoparticles. *J. Am. Chem. Soc.* **2022**, *144*, 7919−7928.
(34) Xin, H. L.; Niu, K.; Alsem, D. H.; Zheng, H. In Situ TEM Study of Catalytic Nanoparticle Reactions in Atmospheric Pressure Gas Environment. *Microsc. Microanal.* **2013**, *19*, 1558−1568.
(35) Nilsson, S.; Albinsson, D.; Antosiewicz, T. J.; Fritzsche, J.; Langhammer, C. Resolving Single Cu Nanoparticle Oxidation and Kirkendall Void Formation with in Situ Plasmonic Nanospectroscopy and Electrodynamic Simulations. *Nanoscale* **2019**, *11*, 20725−20733.
(36) Cargnello, M.; Chen, C.; Diroll, B. T.; Doan-Nguyen, V. V. T.; Gorte, R. J.; Murray, C. B. Efficient Removal of Organic Ligands from Supported Nanocrystals by Fast Thermal Annealing Enables Catalytic Studies on Well-Defined Active Phases. *J. Am. Chem. Soc.* **2015**, *137*, 6906−6911.
(37) Foucher, A. C.; Marcella, N.; Lee, J. D.; Tappero, R.; Murray, C. B.; Frenkel, A. I.; Stach, E. A. Dynamical Change of Valence States and Structure in $NiCu_3$ Nanoparticles during Redox Cycling. *J. Phys. Chem. C* **2022**, *126*, 1991−2002.
(38) Luneau, M.; Guan, E.; Chen, W.; Foucher, A. C.; Marcella, N.; Shirman, T.; Verbart, D. M. A.; Aizenberg, J.; Aizenberg, M.; Stach, E. A.; Madix, R. J.; Frenkel, A. I.; Friend, C. M. Enhancing Catalytic Performance of Dilute Metal Alloy Nanomaterials. *Commun. Chem.* **2020**, *3*, No. 46.
(39) Ravel, B.; Newville, M. ATHENA, ARTEMIS, HEPHAESTUS: Data Analysis for X-Ray Absorption Spectroscopy Using IFEFFIT. *J. Synchrotron Radiat.* **2005**, *12*, 537−541.
(40) Mayrhofer, K. J. J.; Strmcnik, D.; Blizanac, B. B.; Stamenkovic, V.; Arenz, M.; Markovic, N. M. Measurement of Oxygen Reduction Activities via the Rotating Disc Electrode Method: From Pt Model Surfaces to Carbon-Supported High Surface Area Catalysts. *Electrochim. Acta* **2008**, *53*, 3181−3188.
(41) Peng, P.; Lin, X.-M.; Liu, Y.; Filatov, A. S.; Li, D.; Stamenkovic, V. R.; Yang, D.; Prakapenka, V. B.; Lei, A.; Shevchenko, E. V. Binary Transition-Metal Oxide Hollow Nanoparticles for Oxygen Evolution Reaction. *ACS Appl. Mater. Interfaces* **2018**, *10*, 24715−24724.
(42) Jungjohann, K.; Carter, C. B. In Situ and Operando. *Transmission Electron Microscopy*; Springer International Publishing: Berlin, 2016; pp 17−80.
(43) Wang, F.; Kusada, K.; Wu, D.; Yamamoto, T.; Toriyama, T.; Matsumura, S.; Nanba, Y.; Koyama, M.; Kitagawa, H. Solid-Solution Alloy Nanoparticles of the Immiscible Iridium−Copper System with a Wide Composition Range for Enhanced Electrocatalytic Applications. *Angew. Chem.* **2018**, *130*, 4595−4599.
(44) Lee, J. D.; Jishkariani, D.; Zhao, Y.; Najmr, S.; Rosen, D.; Kikkawa, J. M.; Stach, E. A.; Murray, C. B. Tuning the Electrocatalytic Oxygen Reduction Reaction Activity of Pt-Co Nanocrystals by Cobalt Concentration with Atomic-Scale Understanding. *ACS Appl. Mater. Interfaces* **2019**, *11*, 26789−26797.
(45) Benzbiria, N.; Zertoubi, M.; Azzi, M. Oxygen Reduction Reaction Kinetics on Pure Copper in Neutral Sodium Sulfate Solution. *SN Appl. Sci.* **2020**, *2*, 2101.
(46) Goswami, C.; Hazarika, K. K.; Bharali, P. Transition Metal Oxide Nanocatalysts for Oxygen Reduction Reaction. *Mater. Sci. Energy Technol.* **2018**, *1*, 117−128.
(47) Wang, X.; Li, Z.; Qu, Y.; Yuan, T.; Wang, W.; Wu, Y.; Li, Y. Review of Metal Catalysts for Oxygen Reduction Reaction: From Nanoscale Engineering to Atomic Design. *Chem* **2019**, *5*, 1486−1511.
(48) Ye, C. W.; Xu, L. Recent Advances in the Design of a High Performance Metal−Nitrogen−Carbon Catalyst for the Oxygen Reduction Reaction. *J. Mater. Chem. A* **2021**, *9*, 22218−22247.
(49) Ge, X.; Sumboja, A.; Wuu, D.; An, T.; Li, B.; Goh, F. W. T.; Hor, T. S. A.; Zong, Y.; Liu, Z. Oxygen Reduction in Alkaline Media: From Mechanisms to Recent Advances of Catalysts. *ACS Catal.* **2015**, *5*, 4643−4667.
(50) Costa de Oliveira, M. A.; D'Epifanio, A.; Ohnuki, H.; Mecheri, B. Platinum Group Metal-Free Catalysts for Oxygen Reduction Reaction: Applications in Microbial Fuel Cells. *Catalysts* **2020**, *10*, No. 475.
(51) Su, H.; Zhou, W.; Zhou, W.; Li, Y.; Zheng, L.; Zhang, H.; Liu, M.; Zhang, X.; Sun, X.; Xu, Y.; Hu, F.; Zhang, J.; Hu, T.; Liu, Q.; Wei, S. In-Situ Spectroscopic Observation of Dynamic-Coupling Oxygen on Atomically Dispersed Iridium Electrocatalyst for Acidic Water Oxidation. *Nat. Commun.* **2021**, *12*, No. 6118.

https://doi.org/10.1021/acs.chemmater.3c00970
Chem. Mater. 2023, 35, 4572−4580